

SEAGLE: A Scalable Exact Algorithm for Large-Scale Set-based Gene-Environment Interaction Tests in Biobank Data

Jocelyn T. Chi¹, Ilse C. F. Ipsen², Tzu-Hung Hsiao³, Ching-Heng Lin³, Li-San Wang⁴, Wan-Ping Lee⁴, Tzu-Pin Lu⁵, and Jung-Ying Tzeng^{1,5,6*}

¹Department of Statistics, North Carolina State University, Raleigh, NC, USA

²Department of Mathematics, North Carolina State University, Raleigh, NC, USA

³Department of Medical Research, Taichung Veterans General Hospital, Taichung, Taiwan

⁴Department of Pathology and Laboratory Medicine, Perelman School of Medicine, University of Pennsylvania, Philadelphia, PA, USA

⁵Institute of Epidemiology and Preventive Medicine, National Taiwan University, Taipei, Taiwan

⁶Department of Statistics, National Cheng-Kung University, Tainan, Taiwan

Correspondence*:

Jung-Ying Tzeng
jytzeng@ncsu.edu

ABSTRACT

The explosion of biobank data offers immediate opportunities for gene-environment (GxE) interaction studies of complex diseases because of the large sample sizes and the rich collection in genetic and non-genetic information. However, the extremely large sample size also introduces new computational challenges in GxE assessment, especially for set-based GxE variance component (VC) tests, which is a widely used strategy to boost overall GxE signals and to evaluate the joint GxE effect of multiple variants from a biologically meaningful unit (e.g., gene). In this work, focusing on continuous traits, we present SEAGLE, a **S**calable **E**xact **A**lgorithm for **L**arge-scale set-based **GxE** test, to permit GxE VC tests for biobank-scale data. SEAGLE employs modern matrix computations to achieve the same “exact” results as the original GxE VC tests, and does not impose additional assumptions nor relies on approximations. SEAGLE can easily accommodate sample sizes in the order of 10^5 , is implementable on standard laptops, and does not require specialized computing equipment. We demonstrate the performance of SEAGLE using extensive simulations. We illustrate its utility by conducting genome-wide gene-based GxE analysis on the Taiwan Biobank data to explore the interaction of gene and physical activity status on body mass index.

Keywords: **s**calable gene-environment variance component test, **s**calable gene-environment kernel test, **s**calable regional-based gene-environment test

1 INTRODUCTION

Human complex diseases such as neurodegenerative disease, psychiatric disorders, metabolic syndromes and cancers, are complex traits for which disease susceptibility, disease development and treatment response are mediated by intricate genetic and environmental factors. Understanding the genetic etiology of these complex diseases requires collective consideration of potential genetic and environmental contributors. Studies of gene-environment interactions (G×E) enable understanding of the differences that environmental exposures may have on health outcomes in people with varying genotypes [1, 2, 3]. Examples include the impact of physical activity and alcohol consumption on the genetic risk for obesity-related traits [4], the impact of air pollution on the genetic risk for cardio-metabolic and respiratory traits [5], and those examples reviewed in [6].

When assessing G×E effects, set-based tests are popular approaches to detecting interactions between an environmental factor and a set of single nucleotide polymorphism (SNPs) in a gene, sliding window, or functional region [e.g., 7, 8, 9, 10, 11]. Compared to single-SNP G×E tests, set-based G×E tests can enhance testing performance by reducing multiple-testing burden and by aggregating G×E signals over multiple SNPs that are of moderate effect sizes or of low frequencies.

Large-scale biobanks collect genetic and health information of hundreds of thousands of individuals. Their large sample sizes and rich data on non-genetic factors offer unprecedented opportunities for in-depth studies on G×E effects. While the explosion of biobank data collections provides great hopes for novel G×E discoveries, it also introduces computational challenges. In particular, many set-based G×E tests can be cast as variance component (VC) tests under a random effects modeling framework [e.g., 7, 8], including kernel machine based tests [e.g., 9, 12] and similarity regression based methods [e.g., 10, 11]. Hypothesis testing in this framework relies on computations with phenotypic variance matrices with dimension $n \times n$ (with n as the sample size) and may involve estimating nuisance variance components. When n is large, as in the case of biobank data, matrix computations whose operation counts scale with n^3 are prohibitive in terms of computation time and storage.

A number of methods attempt to ease this computational burden by bypassing the estimation of nuisance variance components, either through approximation of the variance or kernel matrices [13] or through approximation of the score-like test statistics [14]. In the first case, approximating the kernel matrices still requires an expensive eigenvalue decomposition upfront, in addition to storage for the explicit formation of the $n \times n$ kernel matrices, thus lacking practical scalability. In the latter case, approximating the test statistics requires assumptions that may or may not be valid and are difficult to validate in practice. Our numerical studies in Section 3 show that the Type 1 error rates and power can be sub-optimal when data do not adhere to the required assumptions.

Here, we focus on continuous traits and introduce a **S**calable **E**xact **A**lgorithm for **L**arge-scale set-based G×E tests (SEAGLE) for performing G×E VC tests on biobank data. Exactness and scalability are achieved through the judicious use of modern matrix computations, allowing us to dispense with approximations and assumptions. More specifically, “exact” refers to the fact that SEAGLE produces the same exact results as the original GxE VC tests in terms of Type 1 error rates and power, rather than the null distribution of the test statistic being asymptotic or exact.

Our numerical experiments illustrate that SEAGLE produces Type 1 error rates and power identical to those of the original GxE VC methods [e.g., 10], but at a fraction of the speed. Additionally, SEAGLE can easily handle biobank-scale data with as many as n individuals in the order of 10^5 , often at the same speed as state-of-the-art approximate methods [14]. Compared with the state-of-the-art approximate method in

[14], SEAGLE can produce more accurate Type 1 error rates and power. Another advantage of SEAGLE is its user-friendliness; it can be run on ordinary laptops and does not require specialized or high performance computing equipment or parallelization. In fact, our timing comparisons in Section 3 were performed on a 2013 Intel Core i5 laptop with a 2.70GHz CPU and 16 GB RAM, specs that are standard for modern laptops. Therefore, SEAGLE makes it possible to run exact and scalable G×E VC tests on biobank-scale data with just a modicum of computational resources.

The rest of the paper proceeds as follows. Section 2 describes the standard mixed effects model G×E effects, testing procedures, computational performance, and SEAGLE algorithm. Section 3 illustrates the performance of SEAGLE using numerical studies. Section 4 concludes with a brief summary of our contributions and avenues for future work.

2 MATERIALS AND METHODS

We describe the standard mixed effects model for G×E effects and testing procedure (Section 2.1), the computational challenges for biobank-scale data (Section 2.2), the components of the SEAGLE algorithm (Section 2.3), and finally the SEAGLE algorithm as a whole (Section 2.3.4).

2.1 GxE Variance Component Tests for Continuous Traits

We present the standard mixed effects model for studying G×E effects, the score-like test statistic, and its p-value. Let $\mathbf{y} \in \mathbb{R}^n$ denote the response vector with n individual responses for a continuous phenotype; $\mathbf{X} \in \mathbb{R}^{n \times p}$ the design matrix of covariates whose leading column is the all ones vector for the intercept; $\mathbf{E} \in \mathbb{R}^n$ the design vector of the environmental factor in the G×E effect; and $\mathbf{G} \in \mathbb{R}^{n \times L}$ the genetic marker matrix with $L < n$. Define the design matrix for the G×E terms as $\tilde{\mathbf{G}} = \text{diag}(\mathbf{E})\mathbf{G} \in \mathbb{R}^{n \times L}$ where $\text{diag}(\mathbf{E}) \in \mathbb{R}^{n \times n}$ is a diagonal matrix with the elements of the vector \mathbf{E} on the diagonal.

Consider the linear mixed effects model [10, 7],

$$\mathbf{y} = \mathbf{X}\beta_X + \mathbf{E}\beta_E + \mathbf{G}\mathbf{b} + \tilde{\mathbf{G}}\mathbf{c} + \boldsymbol{\epsilon}. \quad (1)$$

Here $\beta_X \in \mathbb{R}^p$ and $\beta_E \in \mathbb{R}$ are the fixed-effects coefficients for the covariates and environmental factor, respectively; $\mathbf{b} \in \mathbb{R}^L$ and $\mathbf{c} \in \mathbb{R}^L$ are the genetic main (G) effect and G×E effect, respectively, with $\mathbf{b} \sim N(\mathbf{0}, \tau \mathbf{I}_L)$ and $\mathbf{c} \sim N(\mathbf{0}, \nu \mathbf{I}_L)$; $\boldsymbol{\epsilon} \sim N(\mathbf{0}, \sigma \mathbf{I}_n)$; and $\mathbf{I}_k \in \mathbb{R}^{k \times k}$ denotes the identity matrix of dimension k .

The SNP-set analysis models the G and G×E effects of the L SNPs as random effects rather than fixed effects. This choice avoids power loss for non-small L and numerical difficulties from correlated SNPs that can occur in a fixed effects model. To assess the presence of G×E effects $H_0 : \mathbf{c} = \mathbf{0}$ in model (1), one can apply a score-like test to the corresponding variance component, $H_0 : \nu = 0$.

To simplify the null model of (1) in the score-like test, we consolidate and define $\tilde{\mathbf{X}} = (\mathbf{X} \quad \mathbf{E}) \in \mathbb{R}^{n \times P}$ and $\beta = (\beta_X^T \quad \beta_E^T)^T \in \mathbb{R}^P$, where $P = p + 1$. The resulting null model becomes $\mathbf{y} = \tilde{\mathbf{X}}\beta + \mathbf{G}\mathbf{b} + \boldsymbol{\epsilon}$, where the response is $\mathbf{y} \sim N(\tilde{\mathbf{X}}\beta, \mathbf{V})$ with $\mathbf{V} = \tau \mathbf{G}\mathbf{G}^T + \sigma \mathbf{I}_n$. Following [10], the score-like test statistic is

$$\begin{aligned} T &= \frac{1}{2}(\mathbf{y} - \hat{\boldsymbol{\mu}})^T \mathbf{V}^{-1} \tilde{\mathbf{G}} \tilde{\mathbf{G}}^T \mathbf{V}^{-1} (\mathbf{y} - \hat{\boldsymbol{\mu}}) \\ &= \frac{1}{2} \mathbf{y}^T \mathbf{P} \tilde{\mathbf{G}} \tilde{\mathbf{G}}^T \mathbf{P} \mathbf{y} \equiv \frac{1}{2} \mathbf{t}^T \mathbf{t}, \text{ where } \mathbf{t} = \tilde{\mathbf{G}}^T \mathbf{P} \mathbf{y}. \end{aligned} \quad (2)$$

In Equation (2), $\hat{\mu} = \tilde{\mathbf{X}}\hat{\beta} = \tilde{\mathbf{X}}(\tilde{\mathbf{X}}^T\mathbf{V}^{-1}\tilde{\mathbf{X}})^{-1}\tilde{\mathbf{X}}^T\mathbf{V}^{-1}\mathbf{y}$ and $\mathbf{P} = \mathbf{V}^{-1} - \mathbf{V}^{-1}\tilde{\mathbf{X}}(\tilde{\mathbf{X}}^T\mathbf{V}^{-1}\tilde{\mathbf{X}})^{-1}\tilde{\mathbf{X}}^T\mathbf{V}^{-1}$. Appendix 1 presents the restricted maximum likelihood (REML) expectation-maximization (EM) algorithm for estimating the nuisance VC parameters τ and σ for computing T [10, 11]. The test statistic T follows a weighted $\chi_{(1)}^2$ distribution asymptotically under $H_0 : \nu = 0$. That is, $T \sim \sum_{\ell} \lambda_{\ell} \chi_{(1)}^2$, where λ_{ℓ} 's are the eigenvalues of

$$\mathbf{C} = \mathbf{C}_1 \mathbf{C}_1^T \quad \text{where} \quad \mathbf{C}_1 = \frac{1}{\sqrt{2}} \mathbf{V}^{\frac{1}{2}} \mathbf{P} \tilde{\mathbf{G}}. \quad (3)$$

Given λ_{ℓ} 's, the p-value of T can be computed with the moment matching method in [15] or the exact method in [16].

2.2 Computational Challenges in GxE VC Tests for Biobank-Scale Data

We identify the three computational bottlenecks.

1. The test statistic T and the p-value computation depend on $\mathbf{P} \in \mathbb{R}^{n \times n}$, which in turn depends on $\mathbf{V}^{-1} \in \mathbb{R}^{n \times n}$. Explicit formation of the inverse is too expensive and numerically inadvisable, due to loss of numerical accuracy and stability [17, Chapter 14].
2. The REML EM algorithm (Appendix 1) estimates the nuisance variance components τ and σ in \mathbf{V} under the null hypothesis. Each iteration requires products with the orthogonal projector $\mathbf{I} - \tilde{\mathbf{X}}(\tilde{\mathbf{X}}^T\tilde{\mathbf{X}})^{-1}\tilde{\mathbf{X}}^T$, and inverting a matrix of dimension $n - P \approx n$.
3. Computing the p-values requires two eigenvalue decompositions: (1) an eigenvalue decomposition of \mathbf{V} to compute $\mathbf{V}^{\frac{1}{2}}$ in \mathbf{C}_1 ; and (2) an eigenvalue decomposition of \mathbf{C} to compute λ_{ℓ} 's in the weighted $\chi_{(1)}^2$ distribution. Computing the eigenvalues and eigenvectors of the symmetric matrix $\mathbf{V} \in \mathbb{R}^{n \times n}$ requires $\mathcal{O}(n^3)$ arithmetic operations and $\mathcal{O}(n^3)$ storage. Computing the eigenvalues of $\mathbf{C} \in \mathbb{R}^{n \times n}$ requires another $\mathcal{O}(n^3)$ arithmetic operations.

2.3 Components of the SEAGLE Algorithm for Biobank-Scale GxE VC Test

We present our approach for overcoming the three computational challenges in the previous section: Multiplication with \mathbf{V}^{-1} without explicit formation of the inverse (Section 2.3.1), a scalable REML EM algorithm (Section 2.3.2), and a scalable algorithm for computing the eigenvalues of \mathbf{C} (Section 2.3.3). The idea is to replace explicit formation of inverses by low-rank updates and linear system solutions; and to replace $n \times n$ eigenvalue decompositions with $L \times L$ ones.

2.3.1 Multiplication by \mathbf{V}^{-1} without explicit formation of \mathbf{V}^{-1}

The test statistic T and the p-value depend on \mathbf{V}^{-1} . We avoid the explicit formation of the inverse by viewing $\mathbf{V} = \tau \mathbf{G}\mathbf{G}^T + \sigma \mathbf{I}_n$ as the low-rank update of a diagonal matrix, and then apply the Sherman-Morrison-Woodbury formula below to reduce the dimension of the computed inverse from n to L where $L \ll n$.

LEMMA 1 (Section 2.1.4 in [18]). *Let $\mathbf{H} \in \mathbb{R}^{n \times n}$ be nonsingular, and let $\mathbf{U}, \mathbf{B} \in \mathbb{R}^{n \times L}$ so that $\mathbf{I} + \mathbf{B}^T \mathbf{H}^{-1} \mathbf{U}$ is nonsingular. Then*

$$(\mathbf{H} + \mathbf{U}\mathbf{B}^T)^{-1} = \mathbf{H}^{-1} - \mathbf{H}^{-1}\mathbf{U}(\mathbf{I} + \mathbf{B}^T\mathbf{H}^{-1}\mathbf{U})^{-1}\mathbf{B}^T\mathbf{H}^{-1}.$$

Applying Lemma 1 to the product of the inverse of $\mathbf{V} = \sigma \left(\mathbf{I}_n + \frac{\tau}{\sigma} \mathbf{G} \mathbf{G}^T \right)$ with any right-hand side input $\mathbf{W} \in \mathbb{R}^{n \times l}$ gives

$$\mathbf{V}^{-1} \mathbf{W} = \frac{1}{\sigma} \left[\mathbf{W} - \frac{\tau}{\sigma} \mathbf{G} \left(\mathbf{I}_L + \frac{\tau}{\sigma} \mathbf{G}^T \mathbf{G} \right)^{-1} \mathbf{G}^T \mathbf{W} \right], \quad (4)$$

which reduces the dimension of the inverse from n to L . The explicit computation of the inverse of $\mathbf{M} = \mathbf{I}_L + \frac{\tau}{\sigma} \mathbf{G}^T \mathbf{G} \in \mathbb{R}^{L \times L}$ is, in turn, avoided with a Cholesky decomposition followed by linear system solution. Algorithm 1 shows the pseudocode for computing (4). As a further saving, we pre-compute the Cholesky factorization of \mathbf{M} only once, so it is available for re-use in the computation of the test statistic and p-value,

Algorithm 1 applyVinv

Input: $\mathbf{G} \in \mathbb{R}^{n \times L}$, $\mathbf{W} \in \mathbb{R}^{n \times l}$, $\hat{\tau} > 0$, $\hat{\sigma} > 0$

Output: $\mathbf{V}^{-1} \mathbf{W}$

```

 $\mathbf{M} = \mathbf{I}_L + \frac{\tau}{\sigma} \mathbf{G}^T \mathbf{G}$ 
Cholesky decomposition  $\mathbf{M} = \mathbf{L} \mathbf{L}^T$  //  $\mathbf{L}$  is lower triangular
Solve  $\mathbf{L} \mathbf{X}_1 = \mathbf{G}^T \mathbf{W}$  // Solve lower triangular system for  $\mathbf{X}_1$ 
Solve  $\mathbf{L}^T \mathbf{X}_2 = \mathbf{X}_1$  // Solve upper triangular system for  $\mathbf{X}_2$ 
// to obtain  $\mathbf{X}_2 = \mathbf{M}^{-1} \mathbf{G}^T \mathbf{W}$ 
return  $\mathbf{X} = \frac{1}{\sigma} (\mathbf{W} - \frac{\tau}{\sigma} \mathbf{G} \mathbf{X}_2)$  // Return  $\mathbf{V}^{-1} \mathbf{W}$  as in (4)

```

2.3.2 Scalable REML EM Algorithm

We present the scalable version of the REML EM algorithm in Appendix 1 that avoids explicit formation of the orthogonal projector and the inverses.

We assume throughout that $\tilde{\mathbf{X}}$ has full column rank with $\text{rank}(\tilde{\mathbf{X}}) = P$, and let $\text{range}(\tilde{\mathbf{X}})$ be the space spanned by the columns of $\tilde{\mathbf{X}}$. The space perpendicular to $\text{range}(\tilde{\mathbf{X}})$ is $\text{range}(\tilde{\mathbf{X}})^\perp$, and the orthogonal projector onto this space is

$$\mathbf{A} \mathbf{A}^T = \mathbf{I} - \tilde{\mathbf{X}} (\tilde{\mathbf{X}}^T \tilde{\mathbf{X}})^{-1} \tilde{\mathbf{X}}^T \quad (5)$$

where $\mathbf{A} \in \mathbb{R}^{n \times (n-P)}$ has orthonormal columns with $\mathbf{A}^T \mathbf{A} = \mathbf{I}_{n-P}$. Let $\mathbf{u} = \mathbf{A}^T \mathbf{y} \in \mathbb{R}^{n-P}$ be the orthogonal projection of the response onto $\text{range}(\tilde{\mathbf{X}})^\perp$.

In iteration $t + 1$ of the algorithm, define

$$\hat{\mathbf{R}} = \hat{\tau}_t \mathbf{A}^T \mathbf{G} \mathbf{G}^T \mathbf{A} + \hat{\sigma}_t \mathbf{I}_{n-P} \in \mathbb{R}^{(n-P) \times (n-P)}. \quad (6)$$

Then the updates in (S6) and (S5) from Appendix 1 can be expressed as

$$\begin{aligned} \hat{\tau}_{t+1} &= \frac{\hat{\tau}_t}{L} \left[\hat{\tau}_t \|\mathbf{G}^T \mathbf{A} \hat{\mathbf{R}}^{-1} \mathbf{u}\|_2^2 + \text{trace}(\mathbf{I}_L - \hat{\tau}_t \mathbf{G}^T \mathbf{A} \hat{\mathbf{R}}^{-1} \mathbf{A}^T \mathbf{G}) \right] \\ \hat{\sigma}_{t+1} &= \frac{\hat{\sigma}_t}{n-P} \left[\|\hat{\mathbf{R}}^{-1} \mathbf{u}\|_2^2 + \hat{\tau}_t \text{trace}(\mathbf{G}^T \mathbf{A} \hat{\mathbf{R}}^{-1} \mathbf{A}^T \mathbf{G}) \right]. \end{aligned}$$

The two bottlenecks in the REML EM algorithm are the computation of the non-symmetric ‘square-root’ \mathbf{A} in (5), and products with $\hat{\mathbf{R}}^{-1}$ from (6). Since P is small, $n - P \approx n$, hence explicit formation of the

inverse is out of the question, especially also because $\widehat{\mathbf{R}}$ changes in each iteration due to the change in $\hat{\tau}_t$ and $\hat{\sigma}_t$.

To avoid explicit formation of the full matrix in (5), we compute instead the QR decomposition

$$\tilde{\mathbf{X}} = \underbrace{(\mathbf{Q}_1 \quad \mathbf{Q}_2)}_{\mathbf{Q}} \begin{pmatrix} \mathbf{R}_0 \\ \mathbf{0} \end{pmatrix}, \quad (7)$$

where $\mathbf{Q} \in \mathbb{R}^{n \times n}$ is an orthogonal matrix with $\mathbf{Q}^T \mathbf{Q} = \mathbf{Q} \mathbf{Q}^T = \mathbf{I}_n$. The columns of $\mathbf{Q}_1 \in \mathbb{R}^{n \times P}$ form an orthonormal basis for $\text{range}(\tilde{\mathbf{X}})$, and the columns of $\mathbf{Q}_2 \in \mathbb{R}^{n \times (n-P)}$ form an orthonormal basis for $\text{range}(\tilde{\mathbf{X}})^\perp$. The upper triangular matrix $\mathbf{R}_0 \in \mathbb{R}^{P \times P}$ is nonsingular, due to the assumption of $\tilde{\mathbf{X}}$ having full column rank. Hence (5) simplifies to

$$\mathbf{I} - \tilde{\mathbf{X}}(\tilde{\mathbf{X}}^T \tilde{\mathbf{X}})^{-1} \tilde{\mathbf{X}}^T = \mathbf{I} - \mathbf{Q}_1 \mathbf{Q}_1^T = \mathbf{Q}_2 \mathbf{Q}_2^T.$$

Thus $\mathbf{A} = \mathbf{Q}_2$ represents the trailing $n - P$ columns of the orthogonal matrix \mathbf{Q} in the QR factorization of $\tilde{\mathbf{X}}$.

Algorithm 2 shows pseudocode. Since $\mathbf{A} = \mathbf{Q}_2$ occurs only as \mathbf{A}^T in matrix vector or matrix-matrix multiplications, we do not compute \mathbf{A} explicitly. Instead, we compute the full QR decomposition in (7) where the ‘QR object’ $\mathbf{Q} = (\mathbf{Q}_1 \quad \mathbf{A})$ is stored implicitly in factored form. To compute $\mathbf{u} = \mathbf{A}^T \mathbf{y}$, we multiply $\tilde{\mathbf{u}} = \mathbf{Q}^T \mathbf{y} = \begin{pmatrix} \mathbf{Q}_1^T \mathbf{y} \\ \mathbf{A}^T \mathbf{y} \end{pmatrix}$ and then extract the trailing $n - P$ rows from $\tilde{\mathbf{u}}$.

Furthermore, we apply $\widehat{\mathbf{R}}^{-1}$ from (6) with a modified version of Algorithm 1 where \mathbf{G} is replaced by $\mathbf{A}^T \mathbf{G}$ and \mathbf{I}_n by \mathbf{I}_{n-P} . Unfortunately, one cannot pre-compute a Cholesky factorization for the whole algorithm since $\hat{\tau}_t$ and $\hat{\sigma}_t$ change in each iteration. However, within a single iteration, we pre-compute a Cholesky factorization of $\widehat{\mathbf{R}}$ for subsequent linear system solutions of $\widehat{\mathbf{R}}^{-1} \mathbf{u}$ and $\widehat{\mathbf{R}}^{-1} \mathbf{A}^T \mathbf{G}$. Following previous work on the OVC [10], our convergence criteria are: (i) the magnitude of the relative difference between the current and previous estimate; and (ii) the default convergence tolerance from the SIMreg package for R.

2.3.3 Scalable Algorithm for Computing the Eigenvalues of \mathbf{C}

The computation of the p-values requires the eigenvalues of $\mathbf{C} = \mathbf{C}_1 \mathbf{C}_1^T$ in (3), which in turn involves products with $\mathbf{V}^{\frac{1}{2}} \in \mathbb{R}^{n \times n}$. We avoid the computation of the square root by exploiting the fact that the nonzero eigenvalues of $\mathbf{C}_1 \mathbf{C}_1^T$ are equal to the nonzero eigenvalues of $\mathbf{C}_1^T \mathbf{C}_1$. The symmetry of \mathbf{V} and \mathbf{P} and the equality $\mathbf{P} \mathbf{V} \mathbf{P} = \mathbf{P}$ imply the much simpler expression

$$\mathbf{C}_1^T \mathbf{C}_1 = \frac{1}{2} \tilde{\mathbf{G}}^T \mathbf{P} \mathbf{V} \mathbf{P} \tilde{\mathbf{G}} = \frac{1}{2} \tilde{\mathbf{G}}^T \mathbf{P} \tilde{\mathbf{G}}.$$

The explicit formation of \mathbf{P} is avoided by computing instead products $\mathbf{P} \tilde{\mathbf{G}}$ with Algorithm 1. Therefore, our approach of replacing the $n \times n$ matrix $\mathbf{C}_1 \mathbf{C}_1^T$ with the much smaller $L \times L$ matrix $\mathbf{C}_1^T \mathbf{C}_1$ reduces the operation count from $\mathcal{O}(n^3)$ down to $\mathcal{O}(L^3)$. Part III of Algorithm 3 shows the pseudocode.

Algorithm 2 REML-EM

Input: $\mathbf{y} \in \mathbb{R}^n$, $\mathbf{G} \in \mathbb{R}^{n \times L}$, $\tilde{\mathbf{X}} \in \mathbb{R}^{n \times P}$ $\hat{\tau}_0 > 0$, $\hat{\sigma}_0 > 0$
Output: $\hat{\tau}, \hat{\sigma}$

QR decomposition $\tilde{\mathbf{X}} = \mathbf{Q} \begin{pmatrix} \mathbf{R}_0 \\ \mathbf{0} \end{pmatrix}$	// Compute QR object in QR decomposition of $\tilde{\mathbf{X}}$
Multiply $\tilde{\mathbf{u}} = \mathbf{Q}^T \mathbf{y}$	// Apply <code>qr.qty</code> function to multiply by \mathbf{Q}^T
$\mathbf{u} = \mathbf{A}^T \mathbf{y}$	// Extract trailing $n - P$ rows from $\mathbf{Q}^T \mathbf{y}$
Pre-compute $\mathbf{A}^T \mathbf{G}$	

$t = 0$

while not converged **do**

- Apply $\widehat{\mathbf{R}}^{-1}$ with modified Algorithm 1 and $\hat{\tau}_t$ and $\hat{\sigma}_t$
- $\hat{\tau}_{t+1} = \frac{\hat{\tau}_t}{L} \left[\hat{\tau}_t \|\mathbf{G}^T \mathbf{A} \widehat{\mathbf{R}}^{-1} \mathbf{u}\|_2^2 + \text{trace}(\mathbf{I}_L - \hat{\tau}_t \mathbf{G}^T \mathbf{A} \widehat{\mathbf{R}}^{-1} \mathbf{A}^T \mathbf{G}) \right]$
- $\hat{\sigma}_{t+1} = \frac{\hat{\sigma}_t}{n-P} \left[\|\widehat{\mathbf{R}}^{-1} \mathbf{u}\|_2^2 + \hat{\tau}_t \text{trace}(\mathbf{G}^T \mathbf{A} \widehat{\mathbf{R}}^{-1} \mathbf{A}^T \mathbf{G}) \right]$
- $t = t + 1$

end while

return $\hat{\tau} = \hat{\tau}_{t+1}$, $\hat{\sigma} = \hat{\sigma}_{t+1}$

2.3.4 The SEAGLE Algorithm

Combining the algorithms from Sections 2.3.1–2.3.3 gives the SEAGLE Algorithm 3 for computing the score-like test statistic T and its p -value. SEAGLE is implemented in the publicly available R package SEAGLE.

Algorithm 3 consists of three parts. Part I computes $\hat{\tau}$ and $\hat{\sigma}$ with the scalable REML EM in Algorithm 2; Part II computes the score-like T statistic in (2); and Part III computes the p -values from the eigenvalues of \mathbf{C} in (3). Linear systems with \mathbf{V} are efficiently solved with Algorithm 1. The fast diagonal multiplication in R stores diagonal matrices as vectors. The QR decomposition is implemented with the `qr` function in the R `base` package. The `qr.qty` function makes it possible to left multiply by \mathbf{Q}^T without having to explicitly form \mathbf{Q} .

3 RESULTS

3.1 Simulation Study

We evaluate the performance of our proposed method (SEAGLE) using simulation studies from two settings: I) data simulated from a random effects genetic model with $n = 5,000$ observations, and II) data simulated from a fixed effects genetic model with $n = 20,000$ and $n = 100,000$ observations. In the random effects simulation, we generate data according to Model (1). This enables us to evaluate the estimation and testing performance of SEAGLE. We consider a smaller n to enable comparisons with existing G×E VC tests. In the fixed effects simulation, we generate data from a fixed effects model. This enables us to evaluate the testing performance when the data do not follow our modeling assumptions. We consider larger n values to demonstrate the effectiveness of SEAGLE on biobank-scale data.

In each setting, we study the Type 1 error rate and power. We consider three baseline approaches: (i) the original G×E VC test (referred to as OVC), as implemented in SIMreg [10, 19] (https://www4.stat.ncsu.edu/~jytzeng/software_simreg.php); (ii) fastKM [13]; as implemented in the FastKM R package; and (iii) MAGEE [14]; as implemented in the MAGEE R package.

Algorithm 3 SEAGLE

Input: $\mathbf{y} \in \mathbb{R}^n$, $\tilde{\mathbf{X}} \in \mathbb{R}^{n \times P}$, $\mathbf{E} \in \mathbb{R}^n$, $\mathbf{G} \in \mathbb{R}^{n \times L}$, $\hat{\tau} > 0$, $\hat{\sigma} > 0$
Output: T , p-value

Part I: Compute $\hat{\tau}$ and $\hat{\sigma}$ with the scalable REML EM algorithm

$\hat{\tau}, \hat{\sigma} = \text{REML-EM}(\mathbf{y}, \mathbf{G}, \tilde{\mathbf{X}}, \hat{\tau}_0 > 0, \hat{\sigma}_0 > 0)$ // Algorithm 2 computes estimates for τ and σ

Part II: Compute score-like test statistic T in (2)

```

 $\mathbf{x} = \text{applyVinv}(\mathbf{G}, \hat{\tau}, \hat{\sigma}, \mathbf{y})$  // Algorithm 1 computes  $\mathbf{x} = \mathbf{V}^{-1}\mathbf{y}$ 
 $\mathbf{H} = \text{applyVinv}(\mathbf{G}, \hat{\tau}, \hat{\sigma}, \tilde{\mathbf{X}})$  // Algorithm 1 computes  $\mathbf{H} = \mathbf{V}^{-1}\tilde{\mathbf{X}}$ 
Multiply  $\mathbf{\Gamma} = \tilde{\mathbf{X}}^T \mathbf{H}$  //  $\mathbf{\Gamma} = \tilde{\mathbf{X}}^T \mathbf{V}^{-1} \tilde{\mathbf{X}}$ 
Cholesky decomposition  $\mathbf{\Gamma} = \mathbf{L} \mathbf{L}^T$  //  $\mathbf{L}$  is lower triangular
Solve  $\mathbf{L} \mathbf{c}_1 = \tilde{\mathbf{X}}^T \mathbf{x}$  // Solve lower triangular system for  $\mathbf{c}_1$ 
Solve  $\mathbf{L}^T \mathbf{c}_2 = \mathbf{c}_1$  // Solve upper triangular system for  $\mathbf{c}_2$ 
// to obtain  $\mathbf{c}_2 = (\tilde{\mathbf{X}}^T \mathbf{V}^{-1} \tilde{\mathbf{X}})^{-1} \tilde{\mathbf{X}}^T \mathbf{V}^{-1} \mathbf{y}$ 
 $\mathbf{y}_P = \text{applyVinv}(\mathbf{G}, \hat{\tau}, \hat{\sigma}, \mathbf{y}) - \text{applyVinv}(\mathbf{G}, \hat{\tau}, \hat{\sigma}, \tilde{\mathbf{X}} \mathbf{c}_2)$ 
// Compute  $\mathbf{P}\mathbf{y}$ 
 $\tilde{\mathbf{G}} = \text{diag}(\mathbf{E})\mathbf{G}$ 
Multiply  $\mathbf{t} = \tilde{\mathbf{G}}^T \mathbf{y}_P$ 
return  $T = \frac{1}{2} \mathbf{t}^T \mathbf{t}$ 

```

Part III: Compute p-value from the eigenvalues of \mathbf{C} in (3)

```

 $\mathbf{\Lambda} = \tilde{\mathbf{X}}^T \text{applyVinv}(\mathbf{G}, \hat{\tau}, \hat{\sigma}, \tilde{\mathbf{G}})$  //  $\mathbf{\Lambda} = \tilde{\mathbf{X}}^T \mathbf{V}^{-1} \tilde{\mathbf{G}}$ 
 $\mathbf{L} \mathbf{\Psi}_1 = \mathbf{\Lambda}$  // Solve the lower triangular system for  $\mathbf{\Psi}_1$ 
 $\mathbf{L}^T \mathbf{\Psi}_2 = \mathbf{\Lambda}$  // Solve the upper triangular system for  $\mathbf{\Psi}_2$ , and
// obtain  $\mathbf{\Psi}_2 = \mathbf{\Gamma}^{-1} \mathbf{\Lambda}$ 
 $\mathbf{\Gamma}_1 = \text{applyVinv}(\mathbf{G}, \hat{\tau}, \hat{\sigma}, \tilde{\mathbf{G}}) - \text{applyVinv}(\mathbf{G}, \hat{\tau}, \hat{\sigma}, \tilde{\mathbf{X}} \mathbf{\Psi}_2)$ 
// Compute product  $\mathbf{\Gamma}_1 = \mathbf{P} \tilde{\mathbf{G}}$ 
 $\mathbf{\Gamma}_2 = \frac{1}{2} \tilde{\mathbf{G}} \mathbf{\Gamma}_1$  // Form  $\mathbf{\Gamma}_2 = \mathbf{C}_1^T \mathbf{C}_1$ 
Compute eigenvalues  $\lambda_\ell$ 's of  $\mathbf{\Gamma}_2$  // Compute eigenvalues of  $\mathbf{C}$ 
return p-value computed from  $T$  and  $\lambda_\ell$ 's according to [15] or [16].

```

MAGEE is the state-of-the-art scalable G×E VC test with demonstrated superior performance compared to several set-based GxE methods.

In all simulations, we obtain the genotype design matrix $\mathbf{G} \in \mathbb{R}^{n \times L}$ as follow. First, we employ the COSI software [20] to simulate 10,000 haplotypes of SNP sequences mimicking the European population. We then form a SNP set of L loci with minor allele frequency less than 0.01 by randomly selecting L SNPs without replacement. Finally, in each replicate, we generate the genotypes of n individuals by randomly selecting two haplotypes with replacement. We consider $n = 5,000$ and $L = 100$ in the random effects simulation setting, and $n = 20,000$ or $100,000$ and $L = 100$ or 400 in the fixed effects simulation setting. We also consider a confounding factor $X \in \mathbb{R}^n$ and an environmental factor $E \in \mathbb{R}^n$, and each is generated from a standard normal distribution. Given X and E , we then form the covariate design matrix $\tilde{\mathbf{X}} \in \mathbb{R}^{n \times 3}$ by column-combining the vector of ones, X , and E together.

3.1.1 Random Effects Simulation Study

Given the genotype design matrix \mathbf{G} of $n = 5,000$ and $L = 100$ loci and the $n \times P$ covariate design matrix $\tilde{\mathbf{X}}$ (where $P = 3$), we simulate the outcome data \mathbf{y} according to the random effects model:

$\mathbf{y} = \tilde{\mathbf{X}}\boldsymbol{\beta} + \mathbf{Gb} + \text{diag}(E)\mathbf{Gc} + \mathbf{e}$, where $\boldsymbol{\beta}$ is set as the all ones vector of length P ; \mathbf{b} is generated from $N(\mathbf{0}, \tau \mathbf{I}_L)$; \mathbf{e} is generated from $N(\mathbf{0}, \sigma \mathbf{I}_n)$; σ and τ are set to be 1. We set $\nu = 0$ for Type I error analysis and $\nu > 0$ for power analysis, where the actual value of ν is determined so that the empirical power is not too close to 1. We simulate $N = 1,000$ replicates and evaluate the results at nominal level $\alpha = 0.05$ for all analyses, except in the case of assessing the type I error rate of SEAGLE at $\alpha = 5 \times 10^{-2}, 5 \times 10^{-3}$ and 5×10^{-4} , where we consider $N = 366,000$.

We start with examining the Type 1 error rate for SEAGLE using $N = 366,000$ replicates. Table 1 shows that SEAGLE provides reasonable control over the Type 1 error rate at varying α -levels.

α -Level	Type 1 Error	Std. Error	95% CI
0.05	0.04784	0.00035	(0.04715, 0.04853)
0.005	0.00521	0.00012	(0.00497, 0.00544)
0.0005	0.00067	0.00004	(0.00059, 0.00075)

Table 1. Type 1 error rate with 95% confidence intervals (CIs) for SEAGLE over $N = 366,000$ replicates for $n = 5,000$ observations, $L = 100$ loci, and variance components $\tau = \sigma = 1$ and $\nu = 0$.

Next, under $H_0 : \nu = 0$ and $\tau = \sigma = 1$ with $N = 1,000$ replicates, we compare the testing results of SEAGLE with OVC. Figure 1 (A) shows the bias and the mean square error (MSE) of the estimated values for τ and σ obtained from the SEAGLE and OVC REML EM algorithms. Both algorithms produce very small bias and MSE for τ and σ . Figures 1 (B) and (C) depict scatter plots of the score-like test statistics and p-values, respectively, produced by SEAGLE and OVC. The figures show that SEAGLE and OVC produce identical test statistics and p-values, hence the “exactness” of the SEAGLE algorithm.

		τ	σ
SEAGLE	Bias	-3.06×10^{-4}	-1.01×10^{-3}
	MSE	4.37×10^{-2}	4.18×10^{-4}
OVC	Bias	-6.93×10^{-4}	-5.56×10^{-4}
	MSE	4.36×10^{-2}	1.05×10^{-4}

(A)

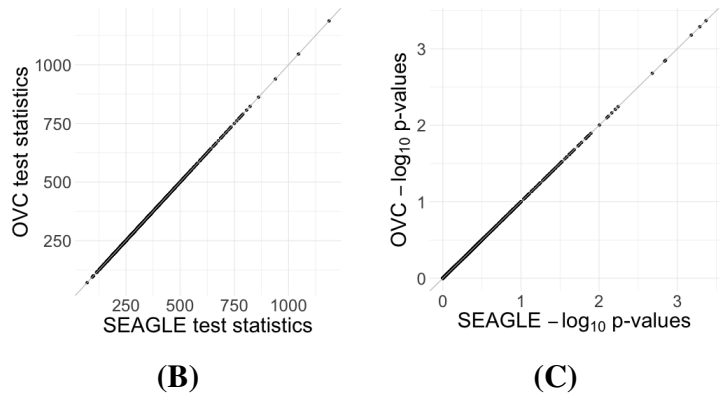
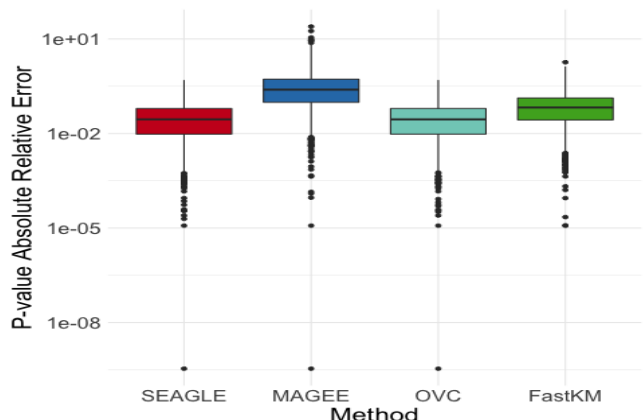


Figure 1. SEAGLE vs. original $G \times E$ VC (OVC) results based on $N = 1,000$ replicates for $n = 5,000$ observations and $L = 100$ loci under $H_0 : \text{no } G \times E \text{ effect } (\nu = 0)$. Panel (A) shows the bias and mean square error (MSE) of the estimated τ and σ values, compared to the true values $\tau = \sigma = 1$. Panels (B) and (C) show the scatter plots of the testing results computed from SEAGLE vs. those from OVC, depicting the exact relationship between SEAGLE and OVC; panel (B) for test statistics T and panel (C) for the p-values.

Since the data are generated from a random effects model under $H_0 : \nu = 0$, we can compute the “true” score-like test statistic T by evaluating (2) at the true τ and σ values, and obtaining the corresponding p-value. We refer to this as the “Truth” and include it as a baseline approach. Supplementary Figure S1 depicts quantile-quantile plots (QQ plots) of the p-values obtained over $N = 1,000$ replicates for Truth, SEAGLE, OVC, FastKM, and MAGEE. All methods exhibit similar p-value behavior, and the red line for

MSE of p-value	
SEAGLE	3.49×10^{-4}
MAGEE	224.96×10^{-4}
OVC	3.49×10^{-4}
FastKM	17.88×10^{-4}

(A)



(B)

Figure 2. Mean square error (MSE; Panel (A)) and absolute relative error (Panel (B)) of the p-values obtained from different GxE VC tests, compared to the “Truth” p-values. Results are obtained with $\tau = \sigma = 1$ under $H_0 : \nu = 0$ over $N = 1,000$ replicates with $n = 5,000$ observations and $L = 100$ loci.

SEAGLE is very close to the light blue (OVC) and yellow lines (Truth). In Figure 2 (A), we also compute the MSE of the p-values obtained from SEAGLE, OVC, FastKM, and MAGEE, compared to the Truth p-values. We observe that MAGEE produces p-values with larger MSE than the other methods. Figure 2 (B) shows the corresponding absolute relative error of the p-values for each method, computed by first taking the absolute difference between a method’s p-value and the Truth p-value, then dividing it by the Truth p-value. The boxplots suggest that MAGEE exhibits higher bias and greater variance than SEAGLE, OVC and FastKM.

Regarding the computational cost, Figure 3 (A) shows boxplots of the computation time in seconds required to obtain a single p-value for each of the methods over $N = 1,000$ replicates with $\tau = \sigma = 1$ and $\nu = 0$. Figure 3 (B) shows the same boxplots for just SEAGLE and MAGEE. Results show that at $n = 5,000$ observations and $L = 100$ loci, SEAGLE is faster than MAGEE on average. All replicates were computed on a 2013 Intel Core i5 laptop with a 2.70GHz CPU and 16 GB RAM.

Figure 4 shows the Type 1 error rate for each method under $H_0 : \nu = 0$. SEAGLE performs identically to OVC with respect to Type 1 error rate at $\alpha = 0.05$ while requiring only a fraction of the computation time, as demonstrated in Figure 3. By contrast, MAGEE is nearly as fast as SEAGLE for $n = 5,000$ and $L = 100$ but produces much more conservative p-values at $\tau = \sigma = 1$.

Figure 5 shows the power for each method under the alternative hypothesis that $\nu > 0$. SEAGLE again performs identically to OVC while requiring a fraction of the computation time. By contrast, MAGEE is nearly as fast as SEAGLE for $n = 5,000$ and $L = 100$ but has lower power when $\tau = \sigma = 1$ and $\nu = 0.04$.

3.1.2 Fixed Effects Simulation Study

To study the performance of our proposed method when the data may not adhere to our model assumptions, we follow previous work [13, 14] and simulate data according to the fixed effects model with a given $\tilde{\mathbf{X}}$ and \mathbf{G} : $\mathbf{y} = \tilde{\mathbf{X}}\boldsymbol{\gamma}_{\tilde{\mathbf{X}}} + \mathbf{G}\boldsymbol{\gamma}_G + \text{diag}(E)\mathbf{G}\boldsymbol{\gamma}_{GE} + \mathbf{e}$, where $\boldsymbol{\gamma}_{\tilde{\mathbf{X}}}$ is the all ones vector of length $P = 3$, $\boldsymbol{\gamma}_G \in \mathbb{R}^L$, $\boldsymbol{\gamma}_{GE} \in \mathbb{R}^L$, and $\mathbf{e} \sim \mathcal{N}(\mathbf{0}, \sigma \mathbf{I}_n)$. The entries of $\boldsymbol{\gamma}_G$ and $\boldsymbol{\gamma}_{GE}$ pertaining to causal loci are set to be γ_G and γ_{GE} , respectively. The remaining entries of $\boldsymbol{\gamma}_G$ and $\boldsymbol{\gamma}_{GE}$ pertaining to non-causal loci are 0. We consider $n = 20,000$ or $100,000$ observations with $L = 100$ or 400 . We select the first ℓ loci to be causal (i.e., loci

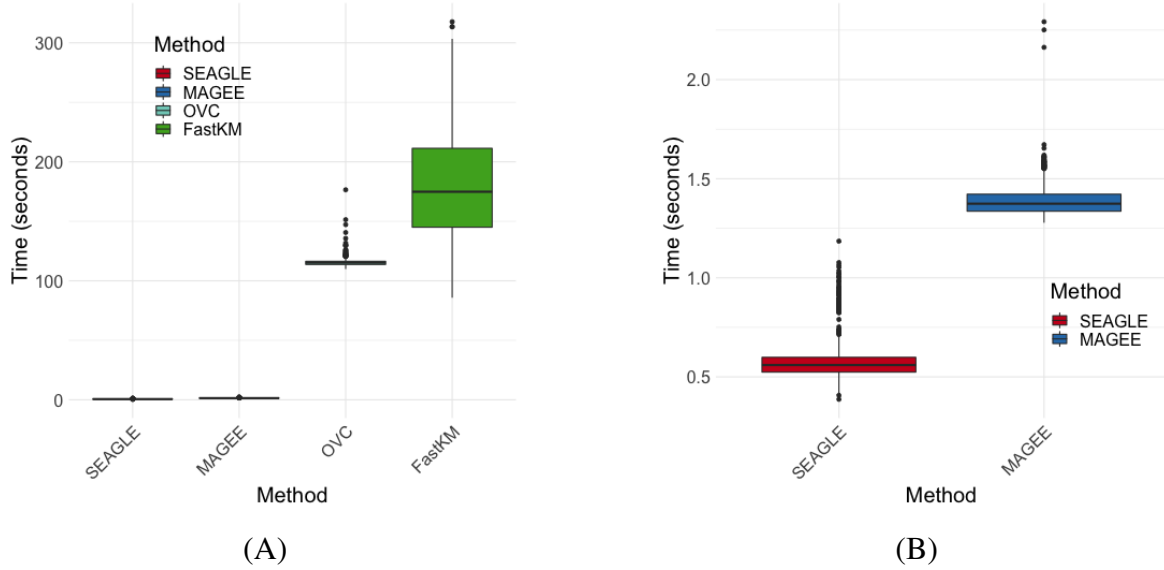


Figure 3. (A) Box plots of computation time in seconds to obtain a single p -value over $N = 1,000$ replicates for $n = 5,000$ observations and $L = 100$ loci. (B) Computation time in seconds to obtain a single p -value for SEAGLE and MAGEE. Replicates computed on a 2013 Intel Core i5 laptop with a 2.70GHz CPU and 16 GB RAM.

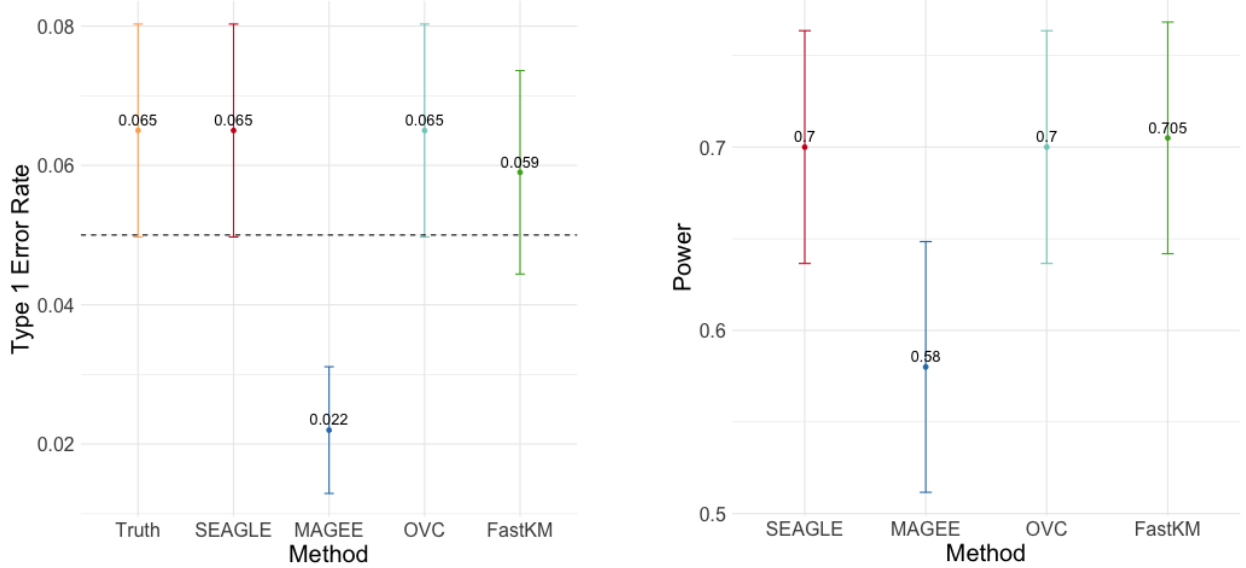


Figure 4. Type 1 error at $\alpha = 0.05$ level for $N = 1,000$ replicates with $n = 5,000$ observations and $L = 100$ loci with $\nu = 0$.

Figure 5. Power at $\alpha = 0.05$ level over $N = 200$ replicates with $n = 5,000$ observations, $L = 100$ loci, and $\nu = 0.04$.

with both G and G×E effects or just G effect). We vary γ_G over 0.5, 1, and 1.5 for the ℓ loci to study the impact of the G main effect sizes. We compare SEAGLE with MAGEE only since OVC and fastKM are unable to work on the sample sizes considered here.

We first evaluate the Type 1 error of SEAGLE by simulating $N = 1,000$ replicates with $L = 100$ for both $n = 20,000$ and $100,000$, and setting $\gamma_{GE} = 0$ for all loci while letting the first $\ell = 40$ loci to have non-zero γ_G . Figure 6 depicts the Type 1 error rate at $\alpha = 0.05$ over varying values for γ_G . While the

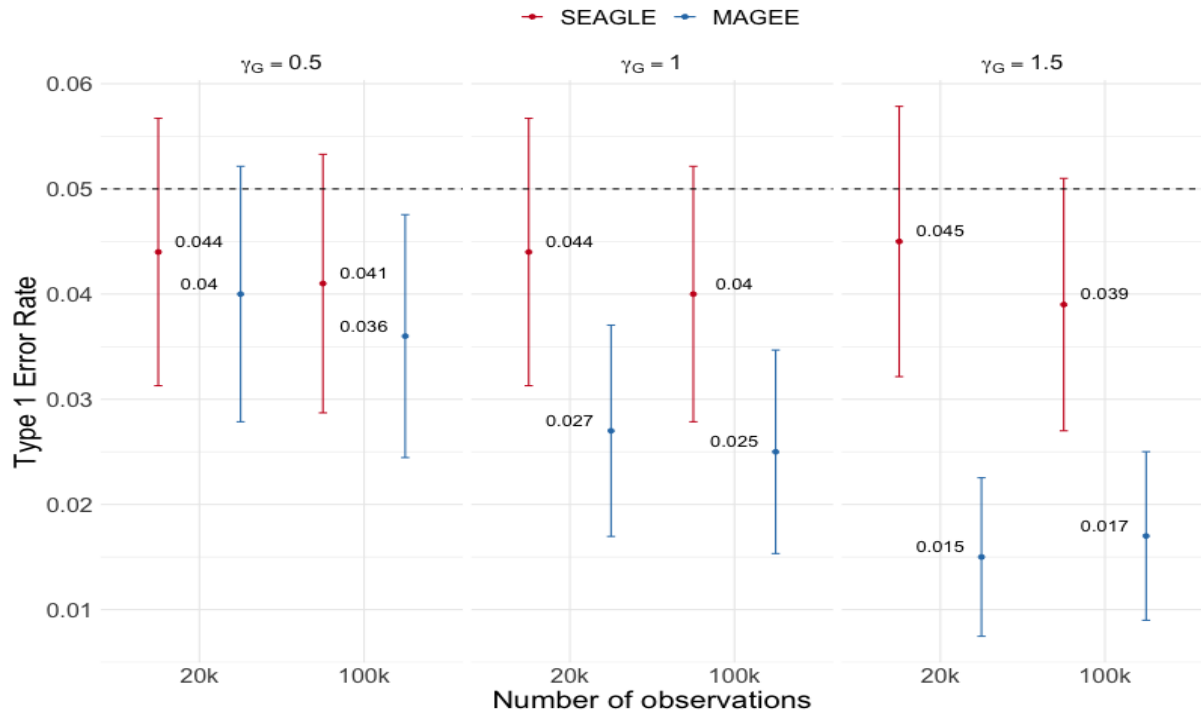


Figure 6. Type 1 error at $\alpha = 0.05$ for fixed effects simulations with $N = 1,000$ replicates with $n = 20,000$ and $n = 100,000$ observations, and $L = 100$ loci with $\gamma_{GE} = 0$ and varying values of γ_G .

Type 1 error rate for SEAGLE remains relatively unaffected by different γ_G values, MAGEE produces more conservative p-values as γ_G increases. This is consistent with the MAGEE assumption requiring a small G main effect [14]. Supplementary Figure S2 shows the corresponding quantile-quantile plots for the p-values obtained from SEAGLE and MAGEE.

Figure 7 depicts boxplots of the computation time in seconds required to obtain a single p-value over the $N = 1,000$ replicates for $n = 20,000$ and $n = 100,000$, and $L = 100$, over varying values for γ_G . All replicates were computed on a 2013 Intel Core i5 laptop with a 2.70GHz CPU and 16 GB RAM. For $n = 20,000$, SEAGLE is faster than MAGEE at larger values of γ_G even though MAGEE computes an approximation to the test statistic T and bypasses the traditional REML EM algorithm. At smaller values of γ_G , however, SEAGLE requires a few seconds more than MAGEE. This is because smaller γ_G values result in smaller τ , and the REML EM algorithm converges slowly for τ values close to 0. Supplementary Figure S3 illustrates this empirically for $n = 20,000$ with the estimated values of τ produced by the REML EM algorithm at different γ_G values. For $n = 100,000$, SEAGLE requires about a second more than MAGEE on average at larger values of γ_G . This is due to the longer time required to estimate τ and σ in the REML EM algorithm for larger n . For smaller values of γ_G , this difference is amplified by the additional EM time required to estimate small values of τ . However, the computation time required for the exact algorithm in SEAGLE at $n = 100,000$ are still comparable to those of the approximate results from MAGEE.

For power evaluation, we simulate $N = 200$ replicates with $L = 100$ and 400, and let the first ℓ causal loci to have non-zero γ_G and γ_{GE} . For $L = 100$ loci, we set γ_{GE} for the first $\ell = 40$ causal loci to be 0.1 or 0.15. For $L = 400$ loci, we set γ_{GE} for the first $\ell = 120$ causal loci to be 0.075 or 0.1. These γ_{GE} values are determined so that the power for $n = 20,000$ at $\alpha = 0.05$ is not close to 1. The values of γ_G for the ℓ causal loci are set to be 0.5, 1.0, and 1.5 as before.

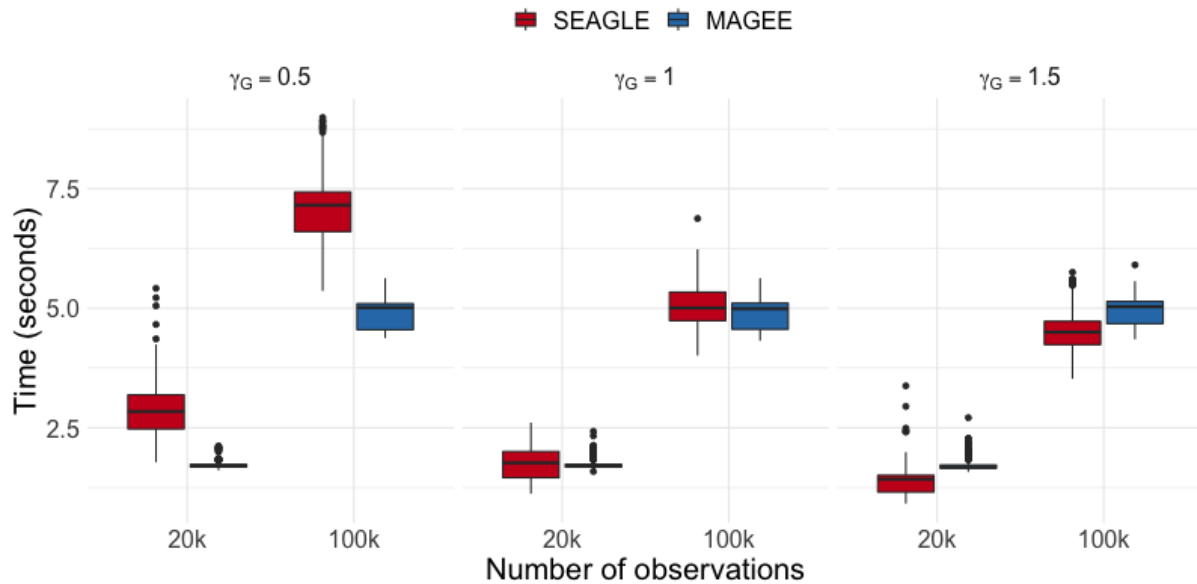


Figure 7. Computation time in seconds for fixed effects simulations with $N = 1,000$ replicates with $n = 20,000$ observations and $L = 100$ loci. Replicates computed on a 2013 Intel Core i5 laptop with a 2.70GHz CPU and 16 GB RAM.

Figure 8 shows the power for $L = 100$ loci. At $n = 20,000$, SEAGLE exhibits better power than MAGEE at all combinations of γ_G and γ_{GE} . Moreover, the difference in power increases for larger values of γ_G since MAGEE relies on the assumption that the G main effect size is small. At $n = 100,000$ and the same values of γ_{GE} , however, both methods produce similar results although SEAGLE still outperforms MAGEE at slightly smaller values of γ_{GE} . Figure 9 shows the power for $L = 400$ loci. Similar patterns of relative power performance are observed as in the case of $L = 100$, except that the power difference between SEAGLE and MAGEE is more pronounced in $L = 400$.

3.2 Application to the Taiwan Biobank Data

To illustrate the scalability of the $G \times E$ VC test using SEAGLE, we apply SEAGLE and MAGEE to the Taiwan Biobank (TWB) data. TWB is a nationwide biobank project initiated in 2012 and has recruited more than 15,995 individuals. Peripheral blood specimens were extracted and genotyped using the Affymetrix Genomewide Axiom TWB array, which was designed specifically for a Taiwanese population. The TWB analysis was approved by the ethical committee at Taichung Veterans General Hospital (IRB TCVGH No. CE16270B-2). We conduct the gene-based $G \times E$ analysis and evaluate the interaction between gene and physical activity (PA) status on body mass index (BMI), adjusting for age, sex and the top 10 principal components for population substructure. The PA status is a binary indicator for with/without regular physical activity. Our $G \times E$ analyses focuses on a subset of 11,664 individuals who have non-missing phenotype and covariate information. The TWB array contains 653,291 SNPs; after PLINK quality control (i.e., removing SNPs with call rates < 0.95 or Hardy-Weinberg Equilibrium p-value $< 10^{-6}$), there are 589,867 SNPs remaining, which are mapped to genes according to the gene range list ‘glist-hg19’ from the PLINK Resources page at <https://www.cog-genomics.org/plink/1.9/resources>. There are a total of 13,260 genes containing more than 1 SNPs for $G \times PA$ interaction analysis.

The median run time of SEAGLE and MAGEE is 2.4 and 1.3 seconds, respectively. Both SEAGLE and MAGEE do not find any significant $G \times PA$ interactions at the genome-wide Bonferroni threshold

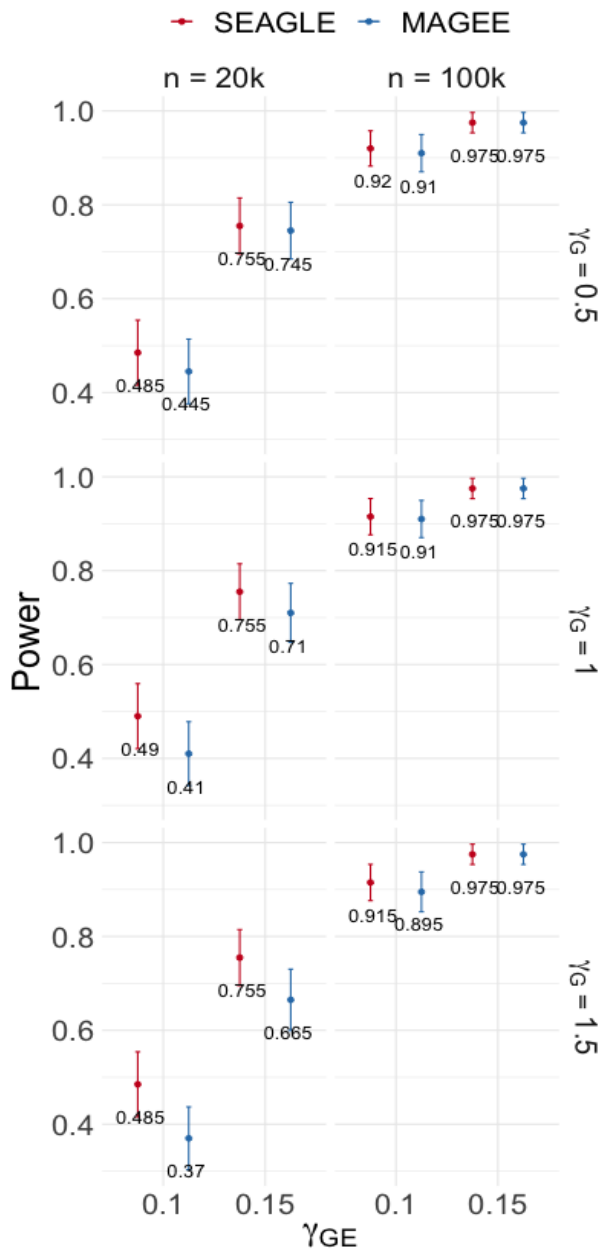


Figure 8. Power at $\alpha = 0.05$ for p -values from fixed genetic effects model over $N = 200$ replicates with $n = 20,000$ and $n = 100,000$ observations and $L = 100$ loci.

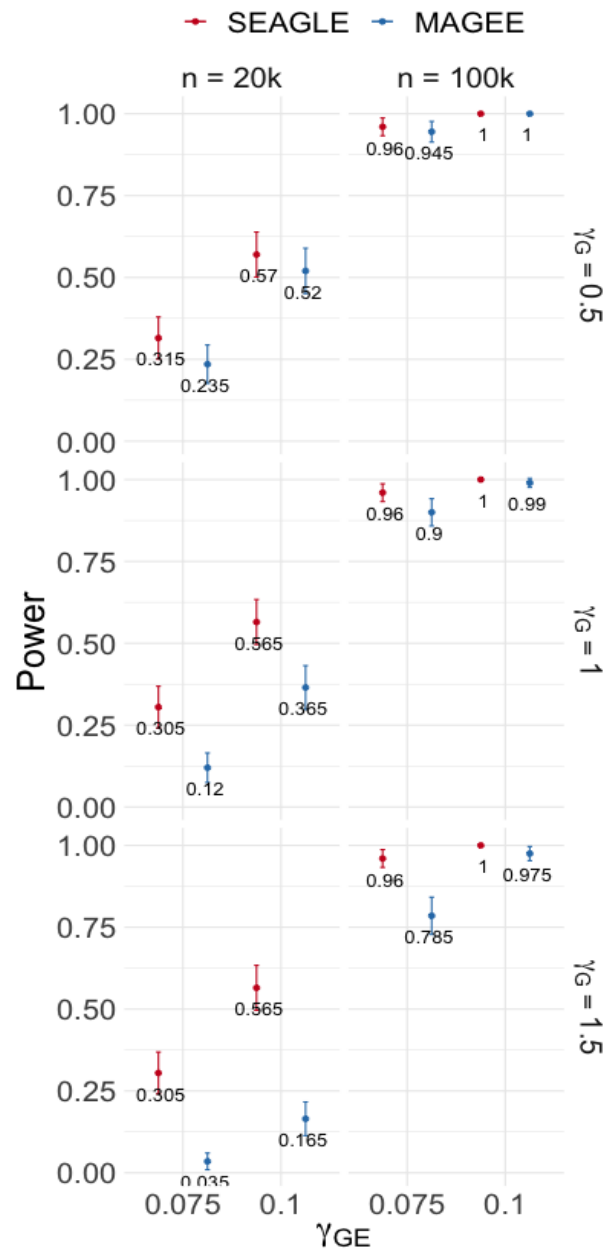


Figure 9. Power at $\alpha = 0.05$ for p -values from fixed genetic effects model over $N = 200$ replicates with $n = 20,000$ and $n = 100,000$ observations and $L = 400$ loci.

$0.05/13,260 = 3.77 \times 10^{-6}$. We hence discuss the results using a less stringent threshold, i.e., 5×10^{-4} and summarize the results in Figure 10 and Supplementary Table S1. SEAGLE and MAGEE identify 8 and 6 G×PA interactions, respectively, among which 5 G×PA results are identified by both methods (Figure 10). The observation that SEAGLE identifies slightly more G×PA effects than MAGEE generally agrees with the simulation findings. We use the GeneCards Human Gene Database (www.genecards.org) [21] to explore the relevance of the identified genes with BMI or PA (see Supplementary Tables S1). Two of the 5 commonly identified genes, i.e., *FCN2* and *OCM*, have non-zero relevance scores (i.e., 0.56 and 0.91,

respectively). For the 3 genes identified by SEAGLE only, i.e., *ALOX5AP*, *BCLAF1* and *PCDH17*, their relevance scores are 6.16, 0.26 and 1.54, respectively. The expression of *ALOX5AP* has also been found associated with obesity and insulin resistance [22] as well as exercise-induced stress [23]. On the other hand, *TBPL1* (identified by MAGEE only) is not in the GeneCards relevance list with BMI or PA.

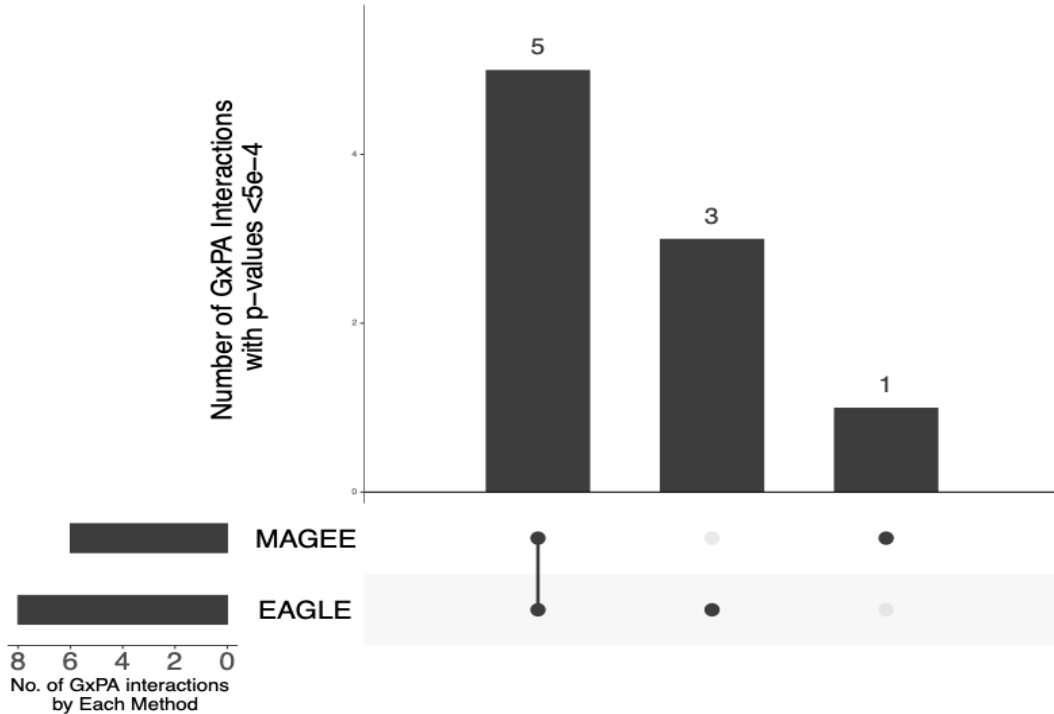


Figure 10. Upset plot of significant $G \times PA$ interactions identified by SEAGLE and MAGEE in the Taiwan Biobank at the 5×10^{-4} nominal level.

4 DISCUSSION

We introduced SEAGLE, a scalable exact algorithm for performing set-based $G \times E$ VC tests on large-scale biobank data. We achieve scalability and accuracy by applying modern numerical analysis techniques, which include avoiding the explicit formation of products and inverses of large matrices. Our numerical experiments illustrate that SEAGLE produces Type 1 error rates and power that are identical to those of the original VC test in [10], while requiring a fraction of the computational cost. Moreover, SEAGLE is well-equipped to handle the very large dimensions required for analysis of large-scale biobank data.

State-of-the-art computational approaches such as MAGEE bypass the traditional time-consuming REML EM algorithm, and instead compute an approximation to the score-like test statistic by assuming that the G main effect size is small. In practice, however, the G main effect size is often unknown. Our numerical experiments illustrate that SEAGLE generally achieves better Type 1 error and power with comparable computation time.

We highlight the fact that our timing experiments were performed on a 2013 Intel Core i5 laptop with a 2.70GHz CPU and 16 GB RAM. Therefore, SEAGLE performs efficient and exact set-based $G \times E$ tests on biobank-scale data with $n = 20,000$ and $n = 100,000$ observations on ordinary laptops, without any need for high performance computational platforms. This makes SEAGLE broadly accessible to all researchers.

Software for SEAGLE is publicly available as the SEAGLE package on GitHub, and will soon be available on the Comprehensive R Archive Network as well.

We conclude with a discussion of three avenues for future extensions. First is the extension of model (1) to generalized linear mixed models that can accommodate binary phenotype traits in addition to the continuous phenotype covered here.

Second is the extension from a single environmental factor to a set of factors represented by $\mathbf{E} \in \mathbb{R}^{n \times q}$ with $q > 1$. The corresponding extension of model (1) is

$$\begin{aligned} \mathbf{y} &= \mathbf{X}\boldsymbol{\beta}_X + \mathbf{h}_E + \mathbf{h}_G + \mathbf{h}_{GE} + \boldsymbol{\epsilon}, \text{ with} \\ \mathbf{h}_E &\sim N(0, \tau_E \boldsymbol{\Sigma}_E), \mathbf{h}_G \sim N(0, \tau_G \boldsymbol{\Sigma}_G), \mathbf{h}_{GE} \sim N(0, \nu \boldsymbol{\Sigma}_{GE}), \text{ and } \boldsymbol{\epsilon} \sim N(0, \sigma \mathbf{I}_n). \end{aligned} \quad (8)$$

Here $\boldsymbol{\Sigma}_E, \boldsymbol{\Sigma}_G, \boldsymbol{\Sigma}_{GE} \in \mathbb{R}^{n \times n}$ are variance matrices, where $\boldsymbol{\Sigma}_E = \mathbf{E}\mathbf{E}^T$, $\boldsymbol{\Sigma}_G = \mathbf{G}\mathbf{G}^T$ and $\boldsymbol{\Sigma}_{GE}$ is the element-wise products of $\boldsymbol{\Sigma}_G$ and $\boldsymbol{\Sigma}_E$. A straightforward adaptation of SEAGLE's scalable REML EM algorithm to the EM algorithm in [19] takes care of estimating the nuisance VC parameters. Numerical analysis techniques analogous to the ones presented here will be the foundation for the efficient extension to multi-E factors.

Third is the extension to other types of kernels [e.g., 19, 24] of the current random effects framework, which can be viewed as a special case of kernel machine regression with linear kernels. As in [25, 26], we will explore the potential of randomized numerical linear algebra, by drawing on the authors' long standing expertise in the development of numerically stable, accurate and efficient randomized matrix algorithms, e.g. [27, 28, 29, 30, 31, 32, 33, 34].

REFERENCES

- [1] Ottman R. Gene–environment interaction: definitions and study design. *Preventive medicine* **25** (1996) 764–770.
- [2] Hunter DJ. Gene–environment interactions in human diseases. *Nature reviews genetics* **6** (2005) 287–298.
- [3] McAllister K, Mechanic LE, Amos C, Aschard H, Blair IA, Chatterjee N, et al. Current challenges and new opportunities for gene-environment interaction studies of complex diseases. *American journal of epidemiology* **186** (2017) 753–761.
- [4] Sulc J, Mounier N, Günther F, Winkler T, Wood AR, Frayling TM, et al. Quantification of the overall contribution of gene-environment interaction for obesity-related traits. *Nature communications* **11** (2020) 1–13.
- [5] Favé MJ, Lamaze FC, Soave D, Hodgkinson A, Gauvin H, Bruat V, et al. Gene-by-environment interactions in urban populations modulate risk phenotypes. *Nature communications* **9** (2018) 1–12.
- [6] Ritz BR, Chatterjee N, Garcia-Closas M, Gauderman WJ, Pierce BL, Kraft P, et al. Lessons learned from past gene-environment interaction successes. *American journal of epidemiology* **186** (2017) 778–786.
- [7] Lin X, Lee S, Christiani DC, Lin X. Test for interactions between a genetic marker set and environment in generalized linear models. *Biostatistics* **14** (2013) 667–681.
- [8] Su YR, Di CZ, Hsu L. A unified powerful set-based test for sequencing data analysis of gxe interactions. *Biostatistics* **18** (2017) 119–131.
- [9] Lin X, Lee S, Wu MC, Wang C, Chen H, Li Z, et al. Test for rare variants by environment interactions in sequencing association studies. *Biometrics* **72** (2016) 156–164.

[10] Tzeng JY, Zhang D, Pongpanich M, Smith C, McCarthy MI, Sale MM, et al. Studying gene and gene-environment effects of uncommon and common variants on continuous traits: a marker-set approach using gene-trait similarity regression. *The American Journal of Human Genetics* **89** (2011) 277–288.

[11] Zhao G, Marceau R, Zhang D, Tzeng JY. Assessing gene-environment interactions for common and rare variants with binary traits using gene-trait similarity regression. *Genetics* **199** (2015) 695–710.

[12] Wang Z, Maity A, Luo Y, Neely ML, Tzeng JY. Complete effect-profile assessment in association studies with multiple genetic and multiple environmental factors. *Genetic epidemiology* **39** (2015) 122–133.

[13] Marceau R, Lu W, Holloway S, Sale MM, Worrall BB, Williams SR, et al. A fast multiple-kernel method with applications to detect gene-environment interaction. *Genetic epidemiology* **39** (2015) 456–468.

[14] Wang X, Lim E, Liu CT, Sung YJ, Rao DC, Morrison AC, et al. Efficient gene-environment interaction tests for large biobank-scale sequencing studies. *Genetic Epidemiology* **44** (2020) 908–923.

[15] Liu H, Tang Y, Zhang HH. A new chi-square approximation to the distribution of non-negative definite quadratic forms in non-central normal variables. *Computational Statistics & Data Analysis* **53** (2009) 853–856.

[16] Davies RB. Algorithm as 155: The distribution of a linear combination of χ^2 random variables. *Applied Statistics* (1980) 323–333.

[17] Higham NJ. *Accuracy and stability of numerical algorithms* (Society for Industrial and Applied Mathematics (SIAM), Philadelphia, PA), second edn. (2002).

[18] Golub GH, Van Loan CF. *Matrix Computations 4th Edition*, vol. 4 (The Johns Hopkins University Press) (2013).

[19] Wang Z, Maity A, Luo Y, Neely ML, Tzeng JY. Complete effect-profile assessment in association studies with multiple genetic and multiple environmental factors. *Genetic epidemiology* **39** (2015) 122–133.

[20] Schaffner SF, Foo C, Gabriel S, Reich D, Daly MJ, Altshuler D. Calibrating a coalescent simulation of human genome sequence variation. *Genome research* **15** (2005) 1576–1583.

[21] Stelzer G, Rosen N, Plaschkes I, Zimmerman S, Twik M, Fishilevich S, et al. The genecards suite: from gene data mining to disease genome sequence analyses. *Current protocols in bioinformatics* **54** (2016) 1–30.

[22] Kaaman M, Rydén M, Axelsson T, Nordström E, Sicard A, Bouloumié A, et al. Alox5ap expression, but not gene haplotypes, is associated with obesity and insulin resistance. *International journal of obesity* **30** (2006) 447–452.

[23] Hilberg T, Deigner HP, Möller E, Claus RA, Ruryk A, Gläser D, et al. Transcription in response to physical stress—clues to the molecular mechanisms of exercise-induced asthma. *The FASEB journal* **19** (2005) 1492–1494.

[24] Broadway KA, Duncan R, Conneely KN, Almli LM, Bradley B, Ressler KJ, et al. Kernel approach for modeling interaction effects in genetic association studies of complex quantitative traits. *Genetic epidemiology* **39** (2015) 366–375.

[25] Lumley T, Brody J, Peloso G, Morrison A, Rice K. Fastskat: Sequence kernel association tests for very large sets of markers. *Genetic epidemiology* **42** (2018) 516–527.

[26] Wu Y, Sankararaman S. A scalable estimator of SNP heritability for biobank-scale data. *Bioinformatics* **34** (2018) i187–i194.

- [27] Chi JT, Ipsen ICF. A projector-based approach to quantifying total and excess uncertainties for sketched linear regression. *submitted* (2020). ArXiv:1808.05924.
- [28] Drineas P, Ipsen ICF. Low-rank approximations do not need a singular value gap. *SIAM J. Matrix Anal. Appl.* **40** (2019) 299–319.
- [29] Eriksson-Bique S, Solbrig M, Stefanelli M, Warkentin S, Abbey R, Ipsen I. Importance sampling for a Monte Carlo matrix multiplication algorithm, with application to information retrieval. *SIAM J. Sci. Comput.* **33** (2011) 1689–1706.
- [30] Holodnak JT, Ipsen ICF. Randomized approximation of the Gram matrix: Exact computation and probabilistic bounds. *SIAM J. Matrix Anal. Appl.* **36** (2015) 110–137.
- [31] Holodnak JT, Ipsen ICF, Smith RC. A probabilistic subspace bound with application to active subspaces. *SIAM J. Matrix Anal. Appl.* **39** (2018) 1208–1220.
- [32] Ipsen ICF, Wentworth T. The effect of coherence on sampling from matrices with orthonormal columns, and preconditioned least squares problems. *SIAM J. Matrix Anal. Appl.* **35** (2014) 1490–1520.
- [33] Saibaba AK, Alexanderian A, Ipsen ICF. Randomized matrix-free trace and log-determinant estimators. *Numer. Math.* **137** (2017) 353–395.
- [34] [Dataset] Wentworth T, Ipsen ICF. Kappa_SQ: A Matlab package for randomized sampling of matrices with orthonormal columns (2014).

CONFLICT OF INTEREST STATEMENT

The authors declare that the research was conducted in the absence of any commercial or financial relationships that could be construed as a potential conflict of interest.